Physics of Plasmas ARTICLE scitation.org/journal/php

Constraining preheat energy deposition in MagLIF experiments with multi-frame shadowgraphy

Cite as: Phys. Plasmas **26**, 032707 (2019); doi: 10.1063/1.5086044
Submitted: 17 December 2018 · Accepted: 17 February 2019 ·
Published Online: 8 March 2019

A. J. Harvey-Thompson,[1,a)] M. Geissel,[1] C. A. Jennings,[1] M. R. Weis,[1] M. R. Gomez,[1] J. R. Fein,[1] D. J. Ampleford,[1] G. A. Chandler,[1] M. E. Glinsky,[1] K. D. Hahn,[1,b)] S. B. Hansen,[1] E. C. Harding,[1] P. F. Knapp,[1] R. R. Paguio,[2] L. Perea,[1] K. J. Peterson,[1] J. L. Porter,[1] P. K. Rambo,[1] G. K. Robertson,[1] G. A. Rochau,[1] C. L. Ruiz,[1] J. Schwarz,[1] J. E. Shores,[1] D. B. Sinars,[1] S. A. Slutz,[1] G. E. Smith,[2] I. C. Smith,[1] C. S. Speas,[1] K. Whittemore,[1] and D. Woodbury[1,3]

AFFILIATIONS

[1]Sandia National Laboratories, P.O. Box 5800, Albuquerque, New Mexico 87185, USA
[2]General Atomics, San Diego, California 92121, USA
[3]University of Maryland, College Park, Maryland 20740, USA

Note: This paper is part of the Special Collection: Papers from the 60th Annual Meeting of the APS Division of Plasma Physics.
Note: Paper KI3 2, Bull. Am. Phys. Soc. **63**, (2018).
[a)]Invited speaker.
[b)]**Current address:** Lawrence Livermore National Laboratory, Livermore, California 94550, USA.

ABSTRACT

A multi-frame shadowgraphy diagnostic has been developed and applied to laser preheat experiments relevant to the Magnetized Liner Inertial Fusion (MagLIF) concept. The diagnostic views the plasma created by laser preheat in MagLIF-relevant gas cells immediately after the laser deposits energy as well as the resulting blast wave evolution later in time. The expansion of the blast wave is modeled with 1D radiation-hydrodynamic simulations that relate the boundary of the blast wave at a given time to the energy deposited into the fuel. This technique is applied to four different preheat protocols that have been used in integrated MagLIF experiments to infer the amount of energy deposited by the laser into the fuel. The results of the integrated MagLIF experiments are compared with those of two-dimensional LASNEX simulations. The best performing shots returned neutron yields ~40–55% of the simulated predictions for three different preheat protocols.

I. INTRODUCTION

In the Magnetized Liner Inertial Fusion (MagLIF) scheme,[1,2] a metallic liner filled with fusion fuel is imploded with the JxB force applied by the Z pulsed power generator (~27 MA, 100 ns current rise time[3]). The typical velocities achieved by pulsed-power-driven implosions are too slow (<100 km/s) to produce fusion-relevant temperatures through adiabatic compression of an initially cold fuel. To overcome this limitation, in MagLIF, the target is initially magnetized with a >10 T axial magnetic field (along the major axis of the cylinder) to suppress thermal conduction from the fuel to the liner walls. The fuel is then heated at the start of the implosion to temperatures of a few hundred eV, referred to as "preheat".

In simulations of integrated MagLIF experiments,[1,4–6] the neutron yield is sensitive to the amount of preheat energy deposited into the fuel at the start of the implosion. Accurately determining the preheat energy is therefore important when assessing the performance of integrated MagLIF experiments. The fuel is preheated with the Z-Beamlet[7] laser: a $\lambda = 527$ nm pulse delivers up to 4 kJ within a few nanoseconds, which enters the target, penetrating a laser entrance hole (LEH) foil that is required to contain the fuel pressure, and deposits energy into the D_2 fuel. In the range of fuel densities currently used (0.7 mg/cm^3–1.05 mg/cm^3), the ratio of electron density to critical density for the laser, $n_e/n_c = 0.05$–0.075, is such that significant energy can be coupled by inverse Bremsstrahlung absorption over the 10 mm imploding height of the target. While the deposition of laser energy into underdense plasmas by inverse bremsstrahlung absorption is generally well understood, the process is complicated substantially if a significant amount of laser energy participates in laser plasma instabilities (LPIs) such as stimulated Brillouin scattering (SBS), stimulated Raman scattering (SRS), and filamentation. In addition, the laser can deposit a significant fraction of its energy into the LEH foil, which is challenging to model accurately and may introduce mix.[8]

While modeling the laser interaction with the LEH foil and the associated laser plasma instabilities is challenging, significant progress is being made. New preheat protocols have been developed iteratively through multiple laser experiments, with the overall direction guided by simulations. This paper will describe MagLIF-relevant gas cell experiments conducted in the Pecos target area[9] that can constrain the energy deposited into the fuel by different preheat protocols. After the Z-beamlet laser (ZBL) deposits energy into the fuel, the plasma is observed to expand as a blast wave, which is imaged with a multi-frame shadowgraphy diagnostic. The blast wave expansion is modeled with one-dimensional (1D) radiation-hydrodynamics simulations which relate the blast wave diameter at a given time to the energy deposited, allowing the total deposited energy to be inferred. This technique is applied to various preheat protocols that have been used in integrated MagLIF experiments on Z.

The different preheat protocols tested couple between 33% and 55% of the incident laser energy onto the target with the primary energy losses being due to SBS backscatter and to heating the LEH foil material.[10] The inferred deposited energies are used to compare integrated experiments with different preheat protocols with scaling curves generated using 2D LASNEX simulations.[4] The neutron yields produced by the best-performing experiments for three of the preheat protocols were within the range of ∼40%–55% of the neutron yields predicted by these simulations.

The structure of this paper is as follows: Sec. II describes the setup of the Pecos experimental chamber where MagLIF-relevant preheat experiments are performed. Section III describes the multi-frame shadowgraphy diagnostic as well as the methodology by which energy depositions are inferred. In Sec. IV, the energies deposited into the fuel by different preheat protocols are assessed and the performance of integrated experiments using those various preheat protocols will be compared with that of simulations. Finally, Sec. V presents conclusions.

II. PECOS CHAMBER EXPERIMENTAL SETUP

To effectively preheat a MagLIF target, the laser needs to deposit energy into the imploding region without introducing mix into the fuel either by direct illumination of the target surface or by injecting the LEH material. The process by which the energy deposition occurs is complicated by the presence of the LEH foil and the potential for LPI. An offline target chamber is used to design and test laser configurations that improve preheat effectiveness. This facility allows for a higher shot rate and unique diagnostics, which are not available on the Z target chamber. The basic setup of the Pecos target chamber is described by Geissel *et al.*[10] The Pecos chamber is one of the five chambers, separated from the Z chamber, into which the ZBL and Z-Petawatt (ZPW[11]) lasers can be directed. The Pecos chamber uses F/10 optics identical to those in Z to deliver ZBL to the center of the target chamber where a variety of MagLIF-relevant experiments can be performed including stand-alone foil transmission experiments[9] or gas cell experiments.

An overview of the gas cell target setup used to test laser preheat configurations is shown in Fig. 1, and a more detailed description of the gas cell targets is given by Geissel *et al.*[10] and Paguio *et al.*[12] The gas cells have an outer diameter (OD) of 38 mm and are 50.8 mm long. This is substantially larger than integrated MagLIF targets (5.58 mm OD, 11.5 mm long) and ensures that the laser energy is deposited into the gas without directly illuminating the walls of the

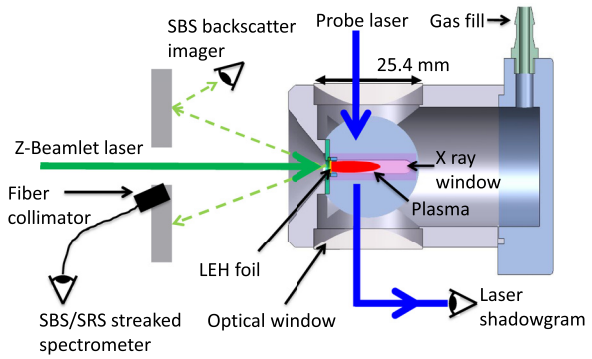

FIG. 1. A drawing illustrating the experimental setup of the gas cell targets in the Pecos chamber including the primary diagnostics.

target. The gas pressure is retained with a polyimide laser entrance hole (LEH) foil window, which is identical to the windows used in integrated MagLIF targets. The laser enters the target through the LEH. The LEH foil dimensions vary depending on the preheat protocol tested. Diagnostic access is provided by four circular 25.4 mm apertures on the sides of the gas cell. Two opposing apertures hold circular, transparent windows that allow an optical probe beam to pass through, while the remaining apertures hold a support structure for a 3 mm wide, 20 mm long, 12.7 μm thick polyimide foil that is transmissive to x-rays. The targets are filled with D_2 gas with a 0.1% (atomic) Ar dopant to pressures up to 120 psi (1.4 mg/cm^3 at room temperature). Typically, the burst pressure for the LEH foil limits the maximum gas pressure that can be used.

The primary diagnostic used to image the plasma produced in the gas cell and constrain energy deposition is a four-frame laser shadowgraphy imager. The diagnostic uses a 2ω (532 nm) optical probe laser that passes through the optical windows on the sides of the target to take shadowgraphy images of the plasma within the gas cell. The probe beam delivers four 600- or 900-ps-long pulses with the first pulse typically timed to the end of the ZBL laser pulse and subsequent pulses separated by 25 ns. The probe laser is imaged using a four-frame optical imager[13] which allows the data to be collected on a single sensor. Each frame is gated for 6.25 ns and co-timed to capture the sub-ns-long pulses of the probe beam. Multiple other diagnostics are also used to observe the heated plasma and assess LPI levels.[10] The amount of light backscattered by SBS and SRS is monitored by imaging a Teflon^{TM} (PTFE) plate that surrounds the entrance aperture through which ZBL enters the chamber with a filtered, time-integrated optical camera at the opposite side of the chamber.[10] The SBS and SRS spectra are also measured using light collected from bare multi-mode fibers positioned to collect backscattered light close to the ZBL aperture which is sent to streaked visible spectrometers. A time integrated x-ray image of the plasma is taken using a side-on x-ray pinhole camera. Finally, an axially resolved (along the ZBL propagation direction), temporally integrated Ar K-shell spectrum is recorded using a spherical crystal spectrometer.[14]

Because the gas cell targets use the same LEH foil design and only minimal dopants in the D_2 gas fill, they are thought to be good surrogates for laser preheat in integrated MagLIF targets. The primary difference is the absence of an applied axial (along the direction of laser propagation) magnetic field which is present in integrated

experiments but not in Pecos. Simulations suggest that a 10 T applied magnetic field (the value used in integrated MagLIF experiments described in this paper) does not significantly affect the energy coupled to the fuel[15] although it can affect the spatial distribution of energy, in particular, by increasing the penetration depth of the laser.

III. CONSTRAINING ENERGY DEPOSITION USING SHADOWGRAPHY

A typical series of shadowgraphs taken each shot is shown in Fig. 2. The first frame is taken immediately after the end of the laser pulse. At this time, the shadowgraphy image shows where the laser has deposited energy into the gas cell and formed a plasma, which produces a dark region (shadow) in the image. The shadow produced by the plasma is a result of a combination of refraction from density gradients at the plasmas' edges and absorption in the plasma volume. For a fully ionized D_2 gas fill at 0.7 mg/cm^3, the electron density is 2.1×10^{20} cm^{-3} corresponding to a ratio of the electron density to critical density of the laser, $n_e/n_{crit} = 0.05$. Simulated shadowgraphy images that include absorption and refraction of the probe beam suggest that the diagnostics observes essentially all plasma produced in the viewed region.

The image at the end of the laser pulse helps constrain the extent of plasma formation by direct laser energy deposition, and the later frames allow the axial distribution of deposited energy to be constrained based on the expansion of the plasma. In order to rapidly process the images and relate the blast wave expansion to a deposited energy, the expansion is modeled with a 1D rad-hydro simulation based on the code GORGON.[16] This approach allows for rapid calculations of the blast wave expansion radius as a function of energy for a given time and initial gas density, both of which can change shot-to-shot. The remainder of this Section will justify this approach and assess the errors and limitations therein.

A. Description of the unfold technique and sensitivities to the model used

To determine the deposited energy consistent with the blast-wave expansion observed by the shadowgraphy diagnostics, 1D radiation hydrodynamic simulations are performed with the code GORGON. The simulations assume that energy is deposited into the plasma in a 3-mm diameter, uniform column over 3 ns. No attempt to model actual laser energy deposition is made during this process. The plasma is allowed to expand during this process and afterwards. This is done for multiple energies producing curves such as the one shown in Fig. 3. These plots can then be used to calculate the energy per unit length as a function of axial distance into the target for a given shadowgraph as shown in Fig. 9. The total energy deposited is calculated by integrating the energy per unit length along the length of the column.

The validity of the modeling assumptions regarding energy deposition and radiation transport was checked using GORGON and HYDRA simulations.[17] The sensitivity of the blast wave radius to various modeling assumptions is shown in Fig. 3. The GORGON curves use atomic emissivity data calculated with Propaceos,[18] and it is assumed that the plasma is optically thin with either pure D_2 or

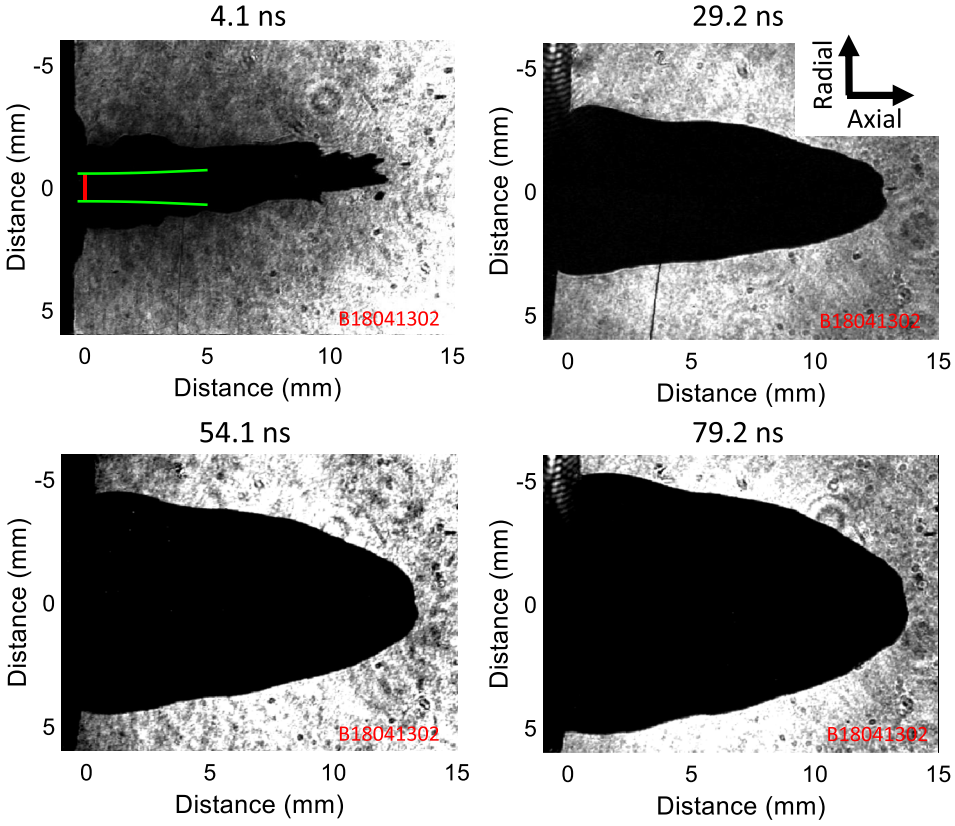

FIG. 2. A series of four shadowgraphy images from shot B18041302 (with the DPP preheat protocol) taken at times after the start of the main pulse indicated. The red line in the top left image at x = 0 mm indicates the initial spot size at the LEH foil, and the green lines indicate the measured beam waist for the distributed phase plate (DPP) smoothed beam. ZBL enters the target from the left. The radial and axial directions used in this paper are illustrated in the top right.

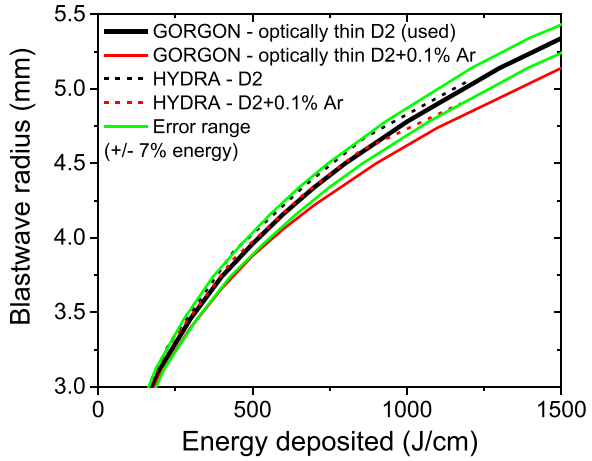

FIG. 3. Comparisons of the blast-wave expansion as a function of energy deposited for different model assumptions.

including the 0.1% Ar dopant. The HYDRA curves, meanwhile, include radiation transport and use DCA opacities. The blast wave radius is identified in GORGON simulations by locating the outermost position where the electron density jumps by a factor of 2, which occurs over a single cell. Differences between the models do exist. In particular, GORGON predicts a larger effect for the 0.1% Ar dopant than HYDRA. We note that it is unclear how accurate radiation models are for Ar at the low temperatures (a few eV) that exist after the laser turns off at the outer edges of the expanded plasma.

For the analysis described in this paper, the model that assumes an optically thin pure D_2 plasma was chosen as it represents a midpoint between the other models and makes reasonable assumptions while being computationally inexpensive to run. A similarly good agreement was found between HYDRA and the optically thin GORGON model for all the shadowgraphy times and densities assessed in this paper. To account for differences in the models plotted in Fig. 3, an uncertainty of $\pm 7\%$ energy per length for a given radius is introduced during the processing.

The simulations suggest that once the expansion has progressed for a sufficiently long time, the expansion radius does not strongly depend on the initial radius into which the energy was deposited, as shown in Fig. 4. This is important because the initial deposition radius is observed to change between experiments depending on the preheat protocol used and also changes with the axial location. The curves used in the analysis assume that energy is deposited in a 3-mm diameter uniform cylinder over 3 ns in all cases.

B. Consistency of unfolds with 2-D simulations

The 1D simulation unfold technique described in Sec. III A assumes that the blast wave expansion is purely radial, whereas there will be some axial component to the blast wave in experiments. To check whether this assumption impacts the inferred energy depositions, a 2D GORGON preheat simulation using a laser ray-trace technique adapted from Ref. 19 was performed for shot B18041201, an experiment using the "*co-injection*" preheat protocol described in Sec. IV A. The simulation used input parameters measured in experiments (laser temporal pulse shape, spatial spot profile, gas fill density, and LEH parameters). Synthetic shadowgraphy images were produced at the same times as experimental shadowgraphy images from this shot. The synthetic shadowgrams accounted for absorption of the probe beam by the plasma and refraction out of the acceptance angle of the relaying optics. The synthetic and experimental shadowgraphy images from this shot are shown in Fig. 5. For this preheat protocol, the simulation reproduced the depth of energy deposition and the observed blast wave expansion well.

The synthetic shadowgraphy images shown in Fig. 6 can now be processed using the energy unfold technique described in Sec. III A to produce energy deposition curves as shown in Fig. 5. In the simulation, of 1681 J energy on the target, 739 J energy was coupled into the foil material and 923 J energy was coupled into the fuel past the LEH location (at $x = 0$ mm). All the synthetic shadowgraphy energy inferences of 919 J, 937 J, and 893 J at 29.2 ns, 54.1 ns, and 79.2 ns are close to the actual energy deposited into the fuel in the simulation. The energies are also close to the experimental values of 888 ± 97 J and 939 ± 101 J deposited into the fuel at 54.1 ns and 79.2 ns, respectively, although the experiments show a slightly shorter penetration depth and a peaked energy deposition profile towards the LEH foil relative to simulations as shown in Fig. 5. This analysis suggests that a 1D unfold, which assumes a purely cylindrical blast-wave, is able to capture energy deposition adequately in these experiments. It also suggests that energy deposited into the LEH foil does not appear in the blast wave unfolds for this preheat protocol. However, the simulations will not capture the energy radiated by the LEH foil which is re-absorbed by the D_2 gas fill because the optically thin model is being used for D_2. More foil material may also be injected into the gas fill region in different preheat protocols that may influence the inferred energy of the blast wave. In this case, the energy can still be thought of as being coupled into the fuel but with an associated increase in LEH foil material mix.

C. Methodology used to infer coupled energies

Applying the 1D blast wave expansion curves to data collected in gas cell experiments requires an accurate knowledge of the image orientation and position relative to the laser propagation. Background images are taken before each experiment using the shadowgraphy diagnostics allowing the initial location of the LEH foil to be located.

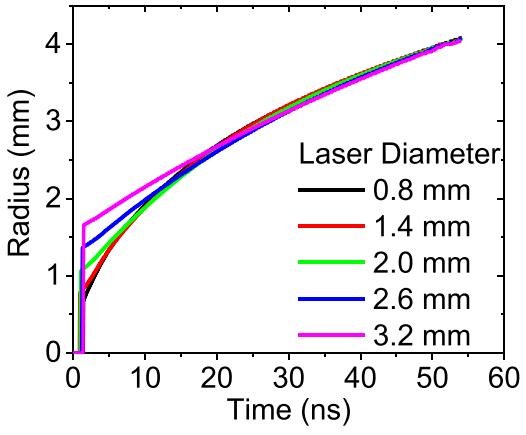

FIG. 4. The blast-wave radius as a function of time for an energy of 1 kJ deposited in different diameter regions in 1D GORGON simulations.

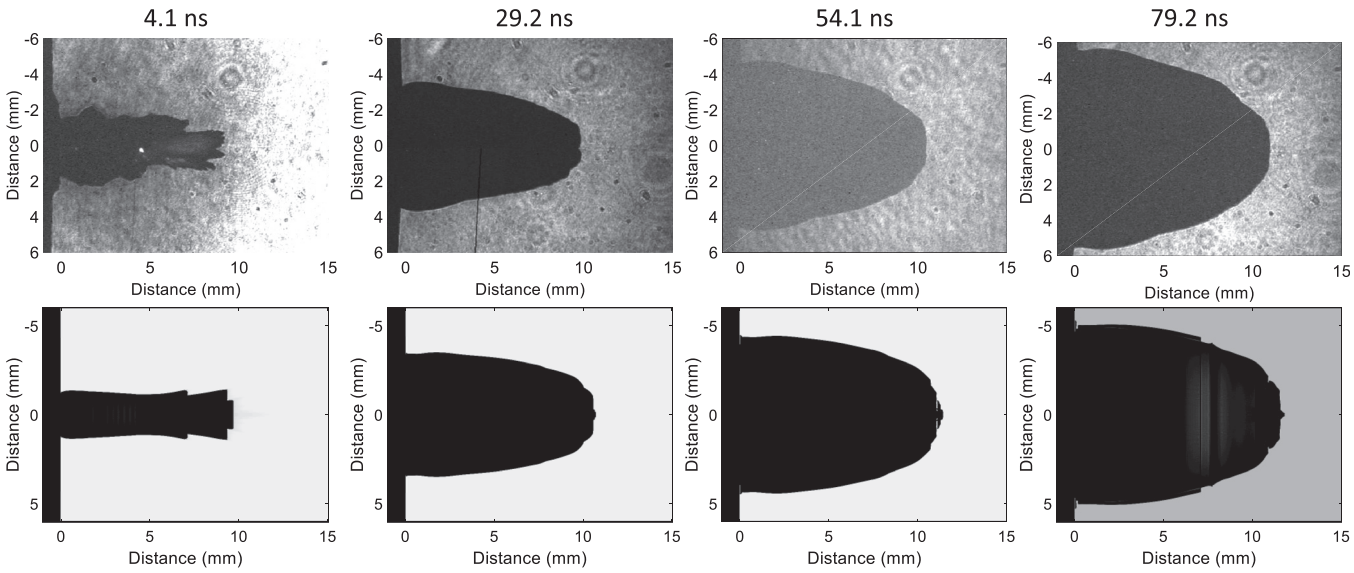

FIG. 5. Experimental (top) and simulated (bottom) shadowgraphy images of shot B18041201, an experiment that used the "co-injection" preheat protocol. The laser enters from the left.

The background image does not give an adequate reference for the center of the blast wave. As discussed in Sec. III, the unfold technique assumes a cylindrical blast wave, and so, the expansion of the blast wave is assumed to be symmetric in the positive and negative y-direction. Given this, the methodology used to determine the energy proceeds as follows: First, the boundary around the blast wave is traced manually with an uncertainty of 2 pixels, as shown in Fig. 7(a). This boundary is then split into top and bottom halves, and the energy as a function of axial distance is calculated based on a simulation run for the experimental parameters (time and gas density) using the optically thin D_2-only GORGON model shown in Fig. 3. At this point, a shift and rotation are applied manually based on the location of the radial midpoint between the boundaries and by matching the energy inferred from the top and bottom boundaries as closely as possible, as illustrated in Fig. 8. Since the mid-point does not follow a straight line and since the energy per length is not a linear function of the blast wave expansion, matching the energy per length curves during this process is required to ensure that the image has been rotated and shifted correctly. The two boundaries generally produce very similar deposition profiles at the end of this process, as illustrated in Fig. 8(c). While this process is repeated for each frame in a given shot, the rotations and shifts are generally the same within $\pm 0.1^\circ$ and $\pm 25\,\mu$m in the vertical direction. The rotations and shifts required are generally $<1^\circ$ and <0.1 mm vertically (the 3.5° rotation applied in Fig. 8 was an outlier). Once the rotation and offset have been determined, the actual energy deposition curve is calculated from the average of the two boundaries. In cases where one of the boundaries cannot be traced back to the position of the LEH, for example, the top boundary after rotation in Fig. 8(b), the "average" location of the boundary reverts to the one that can be traced.

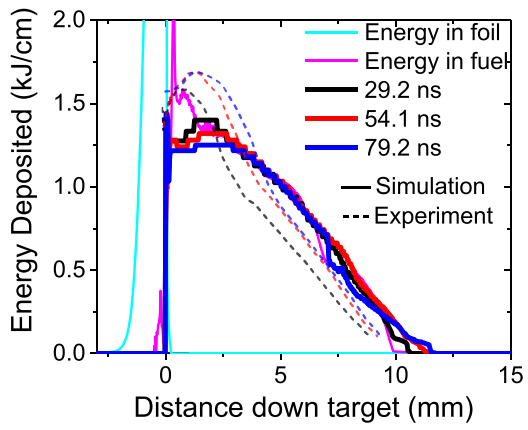

FIG. 6. Plots of the energy deposition into the LEH foil and D_2 gas in a 2D GORGON simulation of shot B18041201 (co-injection protocol) and the energies inferred from analysis of the synthetic and experimental shadowgraphy data from that shot. The peak energy deposited in the foil is 10 kJ/cm.

The error in manually determining the average boundary location is taken to be ± 2 pixels ($\pm 60.8\,\mu$m), as illustrated in Fig. 7(b). The pixel size is $30.4 \pm 0.5\,\mu$m, determined by imaging a 13/16 in.-diameter precision stainless steel ball. The uncertainty in the pixel size is estimated based on observed shot-to-shot variations in this pixel size. The two errors in the boundary location are then added pointwise in quadrature, and the error in the energy is calculated at each axial location based on this (typically $\sim \pm 8\%$). A further $\pm 7\%$ error in the energy, based on model uncertainties shown in Fig. 3, is then added in quadrature to the energy error based on the boundary location uncertainty. The final error in the total measured energy is typically $\sim \pm 11\%$.

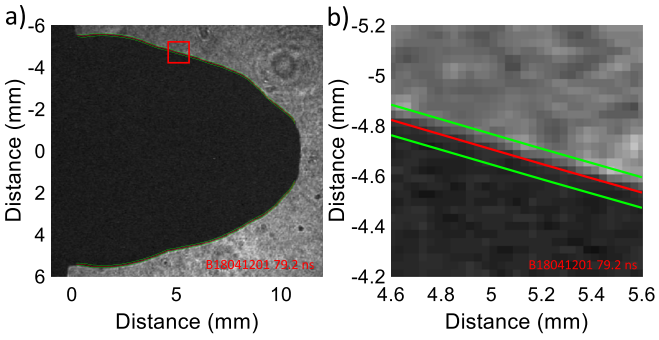

FIG. 7. (a) Shadowgraphy image of B18041201 (co-injection) at 79.2 ns showing the manually traced boundary. The region in the red box is expanded in (b) to show the ±2 pixel uncertainty.

An example of the unfolds generated by this process for the three different frame times from the same shot is shown in Fig. 9. Typically, the energy inferred for the 3rd and 4th shadowgraphy frames at ∼55 ns and ∼80 ns agrees to within <7% of each other, which is within the error bars. However, in some shots, the energy inferred from the second frame at ∼30 ns gives a lower answer for the energy as shown in Fig. 9. The reason for this is not currently known; however, it is possible that the blast wave has not fully developed by 30 ns, in contrast to simulations shown in Fig. 4. For the remainder of this paper, the energy inferred from the frame at ∼55 ns will be used.

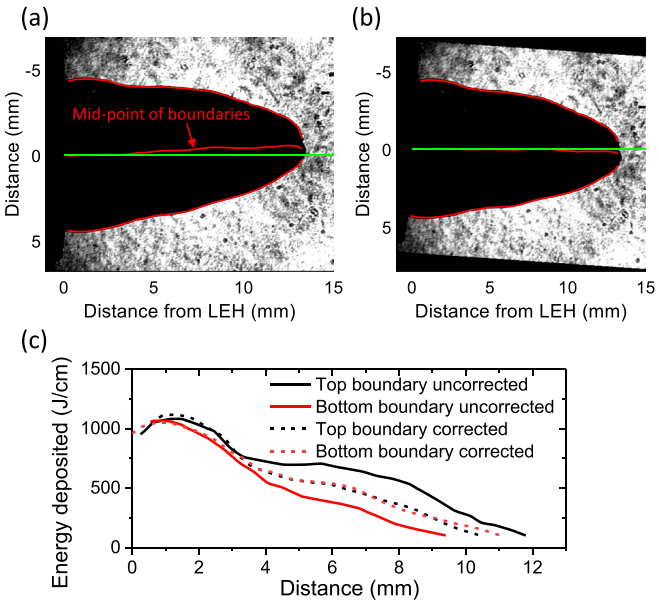

FIG. 8. (a) Original shadowgraphy image at 54.1 ns from B18041302 (co-injection) and (b) that shadowgraph rotated clockwise 3.5° around (0,0). The vertical midpoint between the boundaries is shown in both the cases with a horizontal line for comparison. Figure 8(c) shows how the rotation brings the energy inference from the top and bottom boundaries into closer agreement.

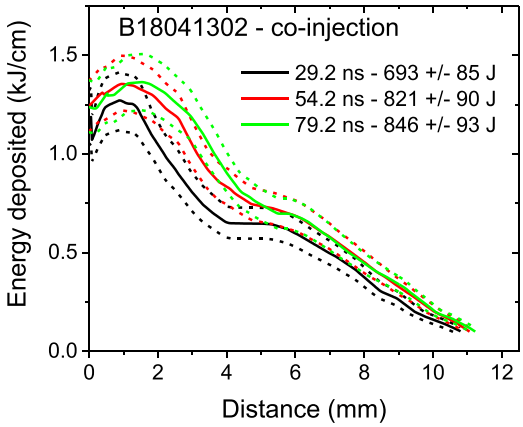

FIG. 9. Energy inferences for the three shadowgraphy frames in shot B18041302. Dashed lines indicate the boundaries including errors.

IV. COMPARISON OF LASER PREHEAT PROTOCOLS

A. Description of protocols tested

Two-dimensional simulations show that the neutron yield produced by MagLIF experiments is strongly dependent on the energy deposited during preheat and on the mix introduced into the fuel at this time.[4,5] The amount of preheat energy deposited and mix introduced is sensitive to a number of laser and target parameters. Many preheat protocols were tested in this study that varied the laser spot size and spatial profile, the LEH foil thickness, the laser temporal pulse shape, and the fuel density. A comprehensive analysis of the dataset will be the subject of a future paper. This paper focuses on the subset of tested protocols that have also been used in integrated MagLIF experiments both before and after the Pecos experimental platform was developed.

A summary of the temporal pulse shapes for the four preheat protocols discussed in this paper is shown in Fig. 10. The first integrated MagLIF experiments used the "*no-DPP, thick window*" preheat protocol, where DPP refers to smoothing by a distributed phase plate. In this case, the LEH foil was 3 mm in diameter and 3.5 μm thick before pressurization. This thickness was intended to enable a gas density of 1.4 mg/cm^3 (120 psi at 293 K) although the first successful experiments using this protocol used only 0.7 mg/cm^3 (60 psi at 293 K).[2,20] In this case, the laser had no DPP smoothing applied and was focused 3.5 mm above the LEH foil producing a focal spot profile shown in Fig. 9(b). The approximate spot envelope in this case was a square ∼500 μm to a side producing a spot-averaged intensity at the LEH foil of ∼4×10^{14} W/cm^2 as presented in Fig. 10(b). The approximate Rayleigh length for this unsmoothed beam is ∼3–5 mm, significantly longer than 280 μm that would be expected if the beam spot were diffraction limited. The pulse shape consisted of a ∼400 J, 0.5 ns pre-pulse, 3.5 ns before an ∼2 kJ main pulse. The intention of the pre-pulse was to heat and rarify the LEH foil material before the main pulse arrived. Since the first MagLIF experiments were successful at 0.7 mg/cm^3, the LEH foil window thickness was reduced in many subsequent experiments to 1.77 μm which is capable of holding the 60 psi fuel pressure.[20] This "*no-DPP, thin window*" protocol was the same as the *no-DPP, thick window* protocol in all other respects. It was

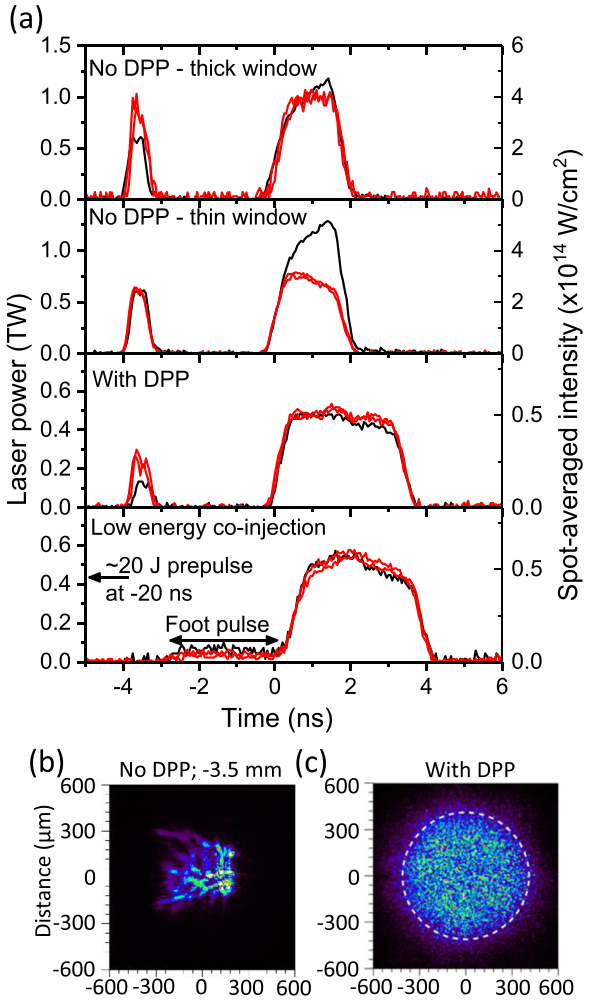

FIG. 10. A summary of (a) the temporal pulse shapes delivered to the targets for the different preheat protocols. The pulse shapes used on integrated MagLIF shots are shown in black, while the equivalent Pecos shots are shown in red. (b) shows a representative image of the spot profile on the LEH foil for the no-DPP protocols, and (c) shows the spot profile produced by the 1100 μm DPP used in the with-DPP and co-injection protocols.

expected that decreasing the LEH foil thickness would increase energy deposition into the fuel.

The no-DPP protocols have significant shortcomings. In particular, it is very challenging to model irregular, unsmoothed spot profiles and the details of the spot profile are sensitive to the condition of optics in the laser chain which may vary over time. In addition, offline foil and gas cell experiments found significant SBS backscatter for the no-DPP protocols due to the high intensities on the target. For these reasons, smoothing with a DPP was applied to produce a 1100-μm diameter spot (containing 95% of the energy) with an 8th order super-Gaussian irradiance profile ($I(r) \propto \exp\left[-2\left(\frac{r}{a}\right)\right]^8$) at best focus, shown in Fig. 10(c), which was positioned at the LEH foil.[10] The lasers' Rayleigh length in this case is 6.6 mm and is determined by the phase plate optic. The measured expansion of the beam waist past the focus containing 95% of the energy is illustrated in Fig. 2. The "*with-DPP*" protocol used this DPP smoothing and slightly modified the temporal pulse shape, shown in Fig. 10(a), to extend the main pulse duration and reduce the main pulse power to minimize SBS backscatter. The pre-pulse energy was reduced to ~80 J, the suggested simulations of which might reduce LEH foil mix, and the main pulse energy was ~1.5 kJ.

Experiments using the *with-DPP* preheat protocol found that a significant amount of LEH foil mix was introduced into the stagnation column in integrated experiments.[8] Simulations suggested that this mix could be mitigated by using an early (−20 ns), low energy (~20 J) pre-pulse that was achieved experimentally by injecting the Z-Petawatt (ZPW) laser in the long-pulse mode along the same beamline as ZBL. The "*co-injection*" protocol used this early pre-pulse and (guided by simulations[8]) shaped the main pulse into a 3 ns, ~0.05 TW foot pulse, intended to slowly reheat the expanded foil material, preceding the ~3.5 ns, 0.5 TW main pulse arrived. For this protocol, the D_2 fuel density was increased to 1.05 mg/cm^3 (90 psi at 293 K, $n_e/n_{crit} = 0.075$), and the diameter of the 1.77 μm LEH foil was reduced to 2 mm to increase the foil robustness to the extra gas pressure. This higher density was intended to reduce the penetration depth of the laser into the target. Higher fuel densities are also predicted to reduce the convergence ratio at peak neutron production in integrated experiments[4] which may lessen the impact of hydrodynamic instability growth on performance. Integrated experiments confirmed that the *co-injection* pulse shape significantly reduced the LEH foil mix as predicted by simulations.[8]

B. Inferred energy coupled

Figure 11 shows shadowgraphy images taken at the end of the main pulse for the four protocols discussed. The plasma produced by the laser interaction has a significantly larger diameter than the spot size on the LEH foil in each case, but particularly for the no-DPP protocols. Notably, the plasma produced in the *no-DPP, thick* window

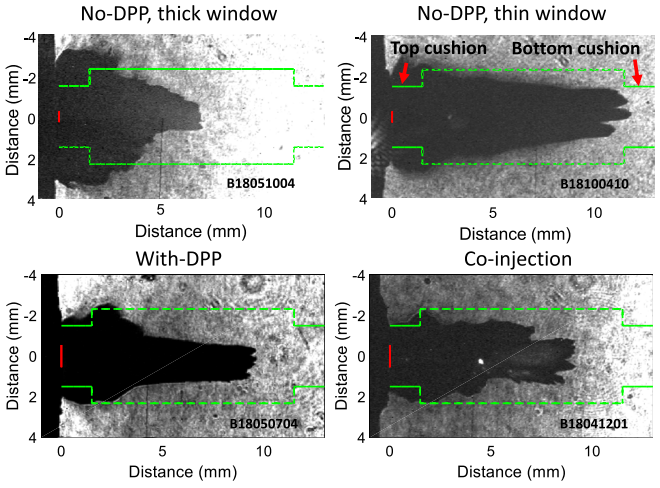

FIG. 11. Shadowgraphy images taken at the end of the main pulse for each of the preheat protocols. The red lines at x = 0 mm indicate the initial spot size at the LEH foil. The green lines represent the location of the interior surface of an integrated MagLIF target. These initial frames are not used to assess the energy deposited.

protocol has a diameter of ∼7 mm. This is likely caused by refraction and filamentation of the laser as it passes through the LEH foil, which may decrease the effective F# of the beam, as has been observed previously in foil transmission experiments.[10] This large deposition radius results in laser energy directly illuminating the inside surfaces of integrated MagLIF targets, whose interior volume is illustrated in Fig. 11, and generating mix. The *no-DPP, thin window*, *with-DPP*, and *co-injection* protocols also penetrate a significant distance into the target where they risk illuminating the top surface of the bottom cushion feature, labelled in Fig. 11, which is used to mitigate magneto-Rayleigh-Taylor (MRT) instability growth.[21] Note that the generation of plasma alone does not necessarily indicate that a significant amount of energy has been deposited at a given location, and thus, the laser energy reaching the bottom cushion may be relatively low.

Unfolds of the energy deposited for each preheat protocol based on the shadowgraphy data taken at ∼55 ns are shown in Fig. 12. Two shots were taken for each preheat protocol, the pulse shapes for which are shown in Fig. 10(a). Some variations in the shape of the energy deposition can be seen between the two shots for the *no-DPP, thick window,* and *co-injection* protocols, in particular, although the total energies deposited between two shots using the same protocol are consistent. There is generally an axial gradient in the energy deposition with more energy being deposited towards the LEH foil, particularly for the *no-DPP, thick window,* and the *with-DPP* protocols. This gradient is to be expected from the inverse Bremsstrahlung absorption process although may be amplified by effects related to the interaction with the LEH foil which decrease the beams' effective F# as described earlier. Since preheat occurs ∼60 ns before stagnation in an integrated MagLIF shot on Z, the deposited energy has sufficient time to be redistributed more uniformly over the fuel volume; however, axial energy gradients may play a role in introducing mix from the top of the target as that redistribution occurs.

The total energy deposited and fraction of incident energy deposited into the fuel for each Pecos experiment, based on the shadowgraphy images, are summarized in Table I. The *no-DPP, thick window* protocol deposits only ∼33% of the on-target energy into the gas. Measurements have shown that a significant fraction of the remaining energy (∼620 J) is lost to SBS backscatter,[10,15] while the remainder is likely lost to heating the LEH foil material.[15] The *no-DPP, thin window* protocol couples ∼55% of the incident energy to the fuel. Compared to the *no-DPP, thick window* protocol, less energy is lost to SBS (∼350 J) and to heating the thinner foil material. Both the *with-DPP* and *co-injection* protocols couple ∼50% of the incident energy to the fuel. Neither of these protocols lose significant energy to SBS backscatter; however, the area of the beam interacting with the LEH foil is significantly larger than for the no-DPP protocols (0.95 mm^2 versus ∼0.3 mm^2 for the no-DPP protocols) and so would be expected to lose significantly more energy to the LEH foil. The dependence between the energy coupled to the LEH foil and the spatial spot size is also seen in LEH-foil-only experiments.[10] The error in the average fraction coupled is taken to be the total spread (including error bars) in the fraction of coupled energy for each configuration.

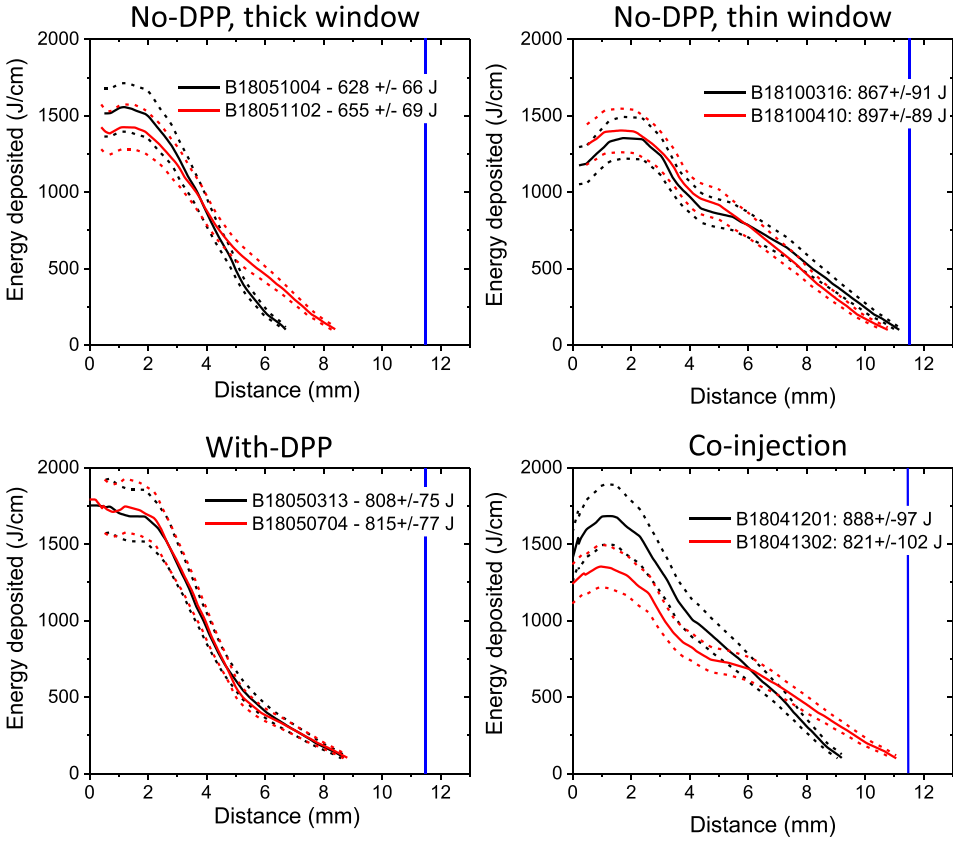

FIG. 12. Energy deposition unfolds from shadowgraphy frames at ∼55 ns for the four different preheat protocols discussed with the total inferred energies for each experiment noted in the legend. Dashed lines represent the maximum and minimum inferred energies.

TABLE I. A summary of the laser spot profile, temporal pulse shape, and early and late-time shadowgraphy data for each of the preheat protocols discussed. The laser energies quoted are those delivered to the target.

Configuration name	Pecos shot number	Pre-pulse (+foot) + main pulse energy (J)	Energy deposited (J)	Fraction coupled	Average fraction coupled
No-DPP, thick window	B18051004	401 + 1642	655±69	0.32±0.03	0.34±0.04
	B18051102	455 + 1679	716±76	0.34±0.04	
No-DPP, thin window	B18100316	348 + 1252	884±93	0.55±0.06	0.55±0.06
	B18100410	324 + 1312	893±94	0.55±0.06	
With-DPP	B18050313	130 + 1563	808±77	0.48±0.04	0.48±0.05
	B18050704	122 + 1552	815±77	0.49±0.05	
Co-injection	B18041201	15 + 92+1574	888±97	0.53±0.06	0.49±0.10
	B18041302	20 + 141+1693	821±102	0.45±0.06	

The amount of energy deposited and the deposition profile for the *no-DPP, thin window,* and *with-DPP* protocols were reproduced for two nominally identical shots. In contrast, the deposition profile for the no-DPP, thick window protocol exhibited significantly more variation which might be a result of the high levels of LPI for this configuration. Surprisingly, the *co-injection* protocol shows the least consistency between the two shots. The reason for this is not entirely understood but may indicate that the energy deposition profile is strongly dependent upon the energy in the foot pulse which varies by ∼50% between the two shots. This variation in the foot pulse energy arises because generating the pulse shape is challenging on ZBL. Experimentally, we do not yet fully understand how sensitive the integrated target performance is to the energy deposition profile. In simulations, there is sufficient time between the preheat phase and stagnation for the energy deposited during preheat to be redistributed throughout the fuel volume.[5] However, differences in the deposition profile may affect mix or how the preheated fuel interacts with the inner surface of the liner.

C. Assessment of integrated performance

In this Section, the neutron yields produced by integrated MagLIF experiments using the preheat protocols described in this paper are compared with quasi-1D simulations to assess the integrated MagLIF performance and the ability of current preheat protocols to couple sufficient energy to the fuel. Table II lists a set of integrated MagLIF experiments performed on Z using the preheat protocols described in this paper. The selected experiments used the same target geometry, applied magnetic field (10 T), and feed geometry that consistently delivers a peak current of ∼16 MA to the load. The target geometry consists of an aspect ratio 6 Be liner (ratio of outer radius to wall thickness) and an inner diameter of 2.325 mm with a 10 mm tall imploding height. All fuel-facing surfaces were made from Be except for the LEH foil. There were some small differences between experiments that are not thought to have a significant effect on this analysis and should not affect the conclusions drawn. In shot z3143, the LEH foil had a 1 nm Co coating on the fuel-facing surface[8] and a 2 ppm Kr dopant was added to the fuel to help constrain mix spectroscopically (<20% effect on yield[4]). In the case of z2839, the LEH foil used was 14% thinner than that in the Pecos experiments (1.52 μm versus 1.77 μm) and the laser energy delivered was greater than that in the Pecos experiments (2360 J versus ∼1600 J in Pecos) which may affect the accuracy of the inferred energy but is very unlikely to affect the conclusions drawn. Only the experiment that produced the highest neutron yield for each preheat protocol is presented here although the repeat dataset is very limited. The energy deposited in the Z shots is calculated based on the fraction of deposited energy in comparable Pecos shots, shown in Table I, multiplied by the total laser energy delivered to the integrated experiment. The neutron yields are determined from several activation detectors (Ref. 22).

Figure 13 shows simulated plots of neutron yield as a function of preheat energy at an applied magnetic field of 10 T for 0.7 mg/cm^3 and

TABLE II. Integrated MagLIF shots using each preheat protocol. The value Y/Y_0 refers to the ratio of the measured yield to that predicted by 2D LASNEX simulations.

Configuration name	Z shot number	Pre-pulse (+foot) + main pulse energy (J)	Energy deposited (J)	Neutron yield ($\times 10^{12}$)	Y/Y_0	
No-DPP, thick window	z2851	342 + 1789	715±75	1.0±0.2	0.15	+0.04 −0.02
No-DPP, thin window	z2839	353 + 2009	1298±145	3.2±0.6	0.43	+0.02 −0.01
With-DPP	z3040	75 + 1551	785±81	4.1±0.8	0.55	+0.09 −0.02
Co-injection	z3143	20 + 183 + 1628	890±180	2.2±0.4	0.4	+0.18 −0.09

1.05 mg/cc fuel densities generated from multiple 2D LASNEX simulations of integrated MagLIF implosions. The setup of the simulations is addressed in detail by Slutz *et al.*[4] The simulations do not model magneto-Rayleigh-Taylor (MRT) instability growth and so can be considered quasi-1D, but do include end-losses and non-ideal Magneto-Hydrodynamic (MHD) terms due to the Hall and Nernst effects. The simulations are driven with a circuit model that captures the current drive in a typical MagLIF experiment. Laser energy is deposited numerically at a fixed power of 1 TW within the 10-mm-long imploding region of the target. The same simulations have predicted that >100 kJ yields should be possible on the Z facility[4] and that very high yields may be possible on future pulsed power facilities.[22] Previous comparisons to simulations before reliable preheat energy deposition data were available suggested that the observed stagnation parameters in early experiments that used the *no-DPP, thick window* preheat protocol were consistent with low preheat energies (100–300 J) being coupled to the fuel.[5] It is therefore interesting to assess how closely the current experimental neutron yields match these simulations and whether sufficient energy is being coupled by preheat to optimize the yield.

The peak simulated yield for a 0.7 mg/cm^3 gas fill is $\sim 8 \times 10^{12}$ neutrons at a deposited energy of ~0.8 kJ. A similar peak yield is found for 1.05 mg/cm^3 gas fills (9.25×10^{12} neutrons) but with the optimum deposited preheat energy increased to ~1.5–2 kJ.[4] An interesting feature of the curves is the decrease in simulated yields at high preheat energies. This occurs because at high simulated preheat energies, the density and temperature gradients within the fuel are increased such that a sufficient magnetic field is advected out of the fuel by the Nernst effect, resulting in reduced thermal insulation. There is, therefore, an optimum preheat energy range that can be targeted to maximize the neutron yield.

Plotted in Fig. 13 are the neutron yields for the integrated Z shots conducted using the different preheat protocols summarized in Table II. The inferred preheat energies deposited for the *with-DPP* and *no-DPP, thick window* preheat protocols come closest to depositing the optimum preheat energy of 700–800 J at a fuel density of 0.7 mg/cm^3. The hypothesis that low preheat energy is responsible for the yields recorded in early experiments is not supported by these data. The *no-DPP, thin window* preheat protocol delivers more energy than optimum. However, in simulations, the yield drops off slowly for deposited energies above the optimum, and so, a greater-than-optimum preheat energy may enable more consistent shot-to-shot performances. By contrast, the energy coupled into the fuel by the *co-injection* protocol (890 ± 180 J) is less than the optimum preheat energy required in simulations for a fuel density of 1.05 mg/cm^3 (~1.5–2 kJ).

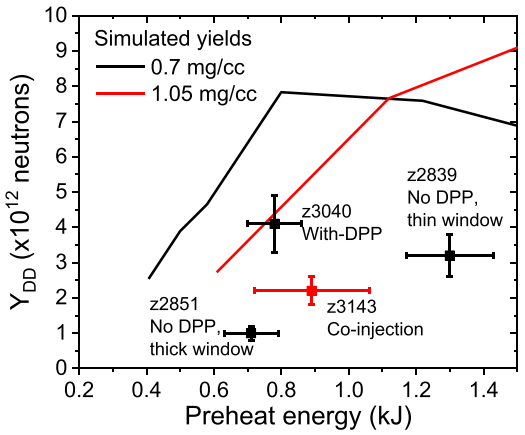

FIG. 13. Simulated curves of neutron yield versus preheat energy generated from a series of 2D LASNEX simulations of integrated experiments. The results from the Z shots listed in Table II are shown for comparison with the simulations.

Table II lists the ratio of the measured neutron yields to the simulated neutron yield for each preheat protocol. The maximum and minimum bounds refer to this ratio for the simulated yields at the maximum and minimum preheat energies for each shot. The poorest performing shot, z2851 using the *no-DPP, thick window* protocol, returned only ~15% of the simulated yield. However, the repeatability of the yield for this specific target and preheat configuration are unknown since only one integrated shot of this type was performed. Other integrated experiments using 7.5 mm tall targets and the *no-DPP, thick window* preheat protocol returned significantly higher DD neutron yields, up to $3.1 \times 10^{12} \pm 20\%$.[15] Experiments using the other preheat protocols all perform relatively similar compared to simulations, between ~0.4 and 0.55, with overlapping error bars. This indicates that performance is relatively consistent between the various preheat protocols for the best-performing shots.

D. Comparisons to other preheat energy inference techniques

Other techniques have previously been used to infer the preheat energy deposition in MagLIF experiments so that comparisons to simulations can be made. Most notably, Slutz *et al.*[4] and Gomez *et al.*[15] used the results from foil-only experiments where the energy transmitted through different LEH foil thicknesses for the no-DPP laser configurations was tested. These experiments[10] included calorimeter measurements for laser energies transmitted along the original F# of the beam and scatter plate measurements for laser energy scattered outside the beam cone. In the study by Gomez *et al.*,[15] the forward propagating energy measured in foil-only experiments was combined with the SBS backscattered energy measured in gas cell experiments and a model for the energy deposited into the LEH foil material was used to account for the total delivered laser energy. Simulations were also used to show that the energy deposited in an LEH foil in foil-only and gas cell experiments was not expected to be significantly different.

Compared to the energy depositions measured using the shadowgraphy technique presented in this paper, in the study by Gomez *et al.*,[15] the coupled energies are somewhat lower for z2851 (*no-DPP, thick window* protocol) at 0.46 (+0.15/−0.29) kJ but are very similar at 1.38 (+0.28/−0.40) kJ for z2839 (*no-DPP, thin window* protocol). The discrepancy between the two techniques in the case of the *no-DPP, thick window* protocol may be the result of additional energy coupled into the LEH foil, which is accounted for in the blast wave measurements, either through the foil material radiating and coupling energy into the fuel or by mixing into the fuel and contributing to the energy in the blast wave. Both these effects are likely to be much more significant for the *no-DPP, thick window* protocol than the *no-DPP, thin window* protocol. Work is ongoing to understand these discrepancies. We note that the differences in coupled energies do not affect the conclusions drawn by Gomez *et al.*[15]

V. CONCLUSIONS

Multi-frame shadowgraphy diagnostics has been developed and applied to MagLIF laser preheat experiments in the Pecos target chamber. The diagnostic images plasma created in the gas cell by laser energy deposition which is found to expand in a blast wave solution after the heating beam turns off. 1D GORGON and HYDRA simulations show similar dependencies on the deposited energy for the blast wave expansion and allow for unfolds of the energy deposition profiles based on the experimental blast wave images. The 1D nature of these unfolds was not found to significantly impact the deposited energy inferred in 2D GORGON laser ray-trace simulations.

The inferred deposited energies were used to assess the performance of integrated experiments using four different preheat protocols. Comparisons to 2D LASNEX simulations showed the best performing shots with most of the protocols returning yields of ~40%–55% of that simulated. The *no-DPP, thick window* preheat protocol was a significant outlier, returning only ~15% of the simulated yield. The consistency of the experimental results compared to simulations may point to some common degradation mechanisms that reduce the yield by a factor of ~2. Possible candidates include MRT growth impacting the stagnation morphology which does have observed non-uniformity and structure,[2] mix introduced by the laser during preheat,[8,23] and liner mix introduced by MRT growth during the deceleration phase.[4,23] Ongoing and future experiments aim to expand the parameter space (current delivery, magnetic field, preheat energy, and fuel density) over which these comparisons can be made to better test the models scaling to future generators.[22] A separate concern, not addressed in this paper, is the reproducibility of the performance (see, e.g., Gomez *et al.*[15,20] and Slutz *et al.*[4] for a more complete dataset) and the factors that affect this which is an ongoing area of research.

The shadowgraphy data suggest that enough energy is being coupled with current preheat protocols to optimize the yield in MagLIF targets with a fuel density of 0.7 mg/cm^3 and an applied magnetic field of 10 T. This is in contrast to some previous work which suggested that low preheat energy may explain the observed stagnation parameters in early experiments.[5] However, future experiments aim to increase the fuel density beyond 1.05 mg/cm^3 and use an applied magnetic field >10 T which requires preheat energies >2 kJ for optimum performance. Currently, a significant amount of energy is lost to the LEH foil material (up to 50%), and the DPP-smoothed protocols that exhibit small amounts of SBS deposit energy over a significant fraction of the target length. Increasing preheat energy deposition without significantly overshooting the bottom of the target will likely require a larger, 1.5-mm-diameter spot size. This, in turn, will increase the amount of LEH foil material that the laser interacts with and so potentially further increase the energy lost to the LEH material. For this reason, it is not currently thought that ZBL can exceed 2 kJ deposited into the fuel with its current parameters (maximum 3 kJ on target) and the current target designs. Options for overcoming this limitation include the planned increase to the lasers' available energy and techniques to reduce the foil thickness, including cryogenically cooling the target to reduce the fuel pressure at a given density[24] and the laser-gate concept.[4]

ACKNOWLEDGMENTS

The authors would like to thank the Z machine operation team, the ZBL operation team, the ABZ operation team, and the target fabrication team for their contributions to this work. We would also like to thank the Laboratory for Laser Energetics for help with designing the distributed phase plate optics used. Sandia National Laboratories is a multi-mission laboratory managed and operated by National Technology and Engineering Solutions of Sandia, LLC., a wholly owned subsidiary of Honeywell International, Inc., for the U.S. Department of Energy's National Nuclear Security Administration under Contract No. DE-NA-0003525. D. Woodbury acknowledges support from the DOE SSGF Program under Grant No. DE-NA0003864. This paper describes the objective technical results and analysis. Any subjective views or opinions that might be expressed in this paper do not necessarily represent the views of the U.S. Department of Energy or the United States Government.

REFERENCES

[1]S. A. Slutz, M. C. Herrmann, R. A. Vesey, A. B. Sefkow, D. B. Sinars, D. C. Rovang, K. J. Peterson, and M. E. Cuneo, Phys. Plasmas **17**, 056303 (2010).
[2]M. R. Gomez, S. A. Slutz, A. B. Sefkow, D. B. Sinars, K. D. Hahn, S. B. Hansen, E. C. Harding, P. F. Knapp, P. F. Schmit, C. A. Jennings, T. J. Awe, M. Geissel, D. C. Rovang, G. A. Chandler, G. W. Cooper, M. E. Cuneo, A. J. Harvey-Thompson, M. C. Herrmann, M. H. Hess, O. Johns, D. C. Lamppa, M. R. Martin, R. D. McBride, K. J. Peterson, J. L. Porter, G. K. Robertson, G. A. Rochau, C. L. Ruiz, M. E. Savage, I. C. Smith, W. A. Stygar, and R. A. Vesey, Phys. Rev. Lett. **113**, 155003 (2014).
[3]M. E. Savage, K. R. LeChien, M. R. Lopez, B. S. Stoltzfus, W. A. Stygar, J. A. Lott, and P. A. Corcoran, in *Proceedings of the Pulsed Power Conference (PPC)* (IEEE, 2011), pp. 983–990.
[4]S. A. Slutz, M. R. Gomez, S. B. Hansen, E. C. Harding, B. T. Hutsel, P. F. Knapp, D. C. Lamppa, T. J. Awe, D. J. Ampleford, D. E. Bliss, G. A. Chandler, M. E. Cuneo, M. Geissel, M. E. Glinsky, A. J. Harvey-Thompson, M. H. Hess, C. A. Jennings, B. Jones, G. R. Laity, M. R. Martin, K. J. Peterson, J. L. Porter, P. K. Rambo, G. A. Rochau, C. L. Ruiz, M. E. Savage, J. Schwarz, P. F. Schmit, G. Shipley, D. B. Sinars, I. C. Smith, R. A. Vesey, and M. R. Weis, Phys. Plasmas **25**, 112706 (2018).
[5]A. B. Sefkow, S. A. Slutz, J. M. Koning, M. M. Marinak, K. J. Peterson, D. B. Sinars, and R. A. Vesey, Phys. Plasmas **21**, 072711 (2014).
[6]R. D. McBride and S. A. Slutz, Phys. Plasmas **22**, 052708 (2015).
[7]P. K. Rambo, I. C. Smith, J. L. Porter, M. J. Hurst, C. S. Speas, R. G. Adams, A. J. Garcia, E. Dawson, B. D. Thurston, C. Wakefield, J. W. Kellogg, M. J. Slattery, H. C. Ives, R. S. Broyles, J. A. Caird, A. C. Erlandson, J. E. Murray, W. C. Behrendt, N. D. Neilsen, and J. M. Narduzzi, Appl. Opt. **44**, 2421 (2005).
[8]A. J. Harvey-Thompson, M. R. Weis, E. C. Harding, M. Geissel, D. J. Ampleford, G. A. Chandler, J. R. Fein, M. E. Glinsky, M. R. Gomez, K. D. Hahn, S. B. Hansen, C. A. Jennings, P. F. Knapp, R. R. Paguio, L. Perea, K. J. Peterson, J. L. Porter, P. K. Rambo, G. K. Robertson, G. A. Rochau, D. E. Ruiz, J. Schwarz, J. E. Shores, D. B. Sinars, S. A. Slutz, G. E. Smith, I. C. Smith, C. S. Speas, and K. Whittemore, Phys. Plasmas **25**, 112705 (2018).
[9]M. Geissel, T. J. Awe, D. E. Bliss, M. E. Campbell, M. R. Gomez, E. Harding, A. J. Harvey-Thompson, S. B. Hansen, C. Jennings, M. W. Kimmel, and others, Proc. SPIE **9731**, 97310O (2016).
[10]M. Geissel, A. J. Harvey-Thompson, T. J. Awe, D. E. Bliss, M. E. Glinsky, M. R. Gomez, E. Harding, S. B. Hansen, C. Jennings, M. W. Kimmel, P. Knapp, S. M. Lewis, K. Peterson, M. Schollmeier, J. Schwarz, J. E. Shores, S. A. Slutz, D. B. Sinars, I. C. Smith, C. S. Speas, R. A. Vesey, M. R. Weis, and J. L. Porter, Phys. Plasmas **25**, 022706 (2018).
[11]J. Schwarz, P. Rambo, M. Geissel, A. Edens, I. Smith, E. Brambrink, M. Kimmel, and B. Atherton, J. Phys. Conf. Ser. **112**, 032020 (2008).
[12]R. R. Paguio, G. E. Smith, J. L. Taylor, K. Tomlinson, R. R. Holt, W. D. Tatum, M. P. Farrell, J. Betcher, A. Harvey-Thompson, M. Geissel, J. Kellogg, and K. Peterson, Fusion Sci. Technol. **73**, 414 (2018).
[13]L. Claus, G. Robertson, L. Fang, R. Kay, M. W. Kimmel, M. Sanchez, J. W. Stahoviak, D. Trotter, and J. L. Porter, Proc. SPIE **9966**, 99660F (2016).
[14]E. C. Harding, T. Ao, J. E. Bailey, G. Loisel, D. B. Sinars, M. Geissel, G. A. Rochau, and I. C. Smith, Rev. Sci. Instrum. **86**, 043504 (2015).
[15]M. R. Gomez, S. A. Slutz, P. F. Knapp, K. D. Hahn, M. R. Weis, E. C. Harding, M. Geissel, J. R. Fein, M. E. Glinsky, S. B. Hansen, A. J. Harvey-Thompson, C. A.

Jennings, I. C. Smith, D. Woodbury, D. J. Ampleford, T. J. Awe, G. A. Chandler, M. H. Hess, D. C. Lamppa, C. E. Myers, C. L. Ruiz, A. B. Sefkow, J. Schwarz, D. A. Yager-Elorriaga, B. Jones, J. L. Porter, K. J. Peterson, R. D. McBride, G. A. Rochau, and D. B. Sinars, IEEE Trans. Plasma Sci. **2019** (published online)
[16]J. P. Chittenden, S. V. Lebedev, C. A. Jennings, S. N. Bland, and A. Ciardi, Plasma Phys. Controlled Fusion **46**, B457 (2004).
[17]M. M. Marinak, G. D. Kerbel, N. A. Gentile, O. Jones, D. Munro, S. Pollaine, T. R. Dittrich, and S. W. Haan, Phys. Plasmas **8**, 2275 (2001).
[18]J. J. MacFarlane, I. E. Golovkin, and P. R. Woodruff, J. Quant. Spectrosc. Radiat. Transfer **99**, 381 (2006).
[19]T. B. Kaiser, Phys. Rev. E **61**, 895 (2000).
[20]M. R. Gomez, S. A. Slutz, A. B. Sefkow, K. D. Hahn, S. B. Hansen, P. F. Knapp, P. F. Schmit, C. L. Ruiz, D. B. Sinars, E. C. Harding, C. A. Jennings, T. J. Awe, M. Geissel, D. C. Rovang, I. C. Smith, G. A. Chandler, G. W. Cooper, M. E. Cuneo, A. J. Harvey-Thompson, M. C. Herrmann, M. H. Hess, D. C. Lamppa, M. R. Martin, R. D. McBride, K. J. Peterson, J. L. Porter, G. A. Rochau, M. E. Savage, D. G. Schroen, W. A. Stygar, and R. A. Vesey, Phys. Plasmas **22**, 056306 (2015).
[21]T. J. Awe, C. A. Jennings, R. D. McBride, M. E. Cuneo, D. C. Lamppa, M. R. Martin, D. C. Rovang, D. B. Sinars, S. A. Slutz, and A. C. Owen, Phys. Plasmas **21**, 056303 (2014).
[22]S. A. Slutz, W. A. Stygar, M. R. Gomez, K. J. Peterson, A. B. Sefkow, D. B. Sinars, R. A. Vesey, E. M. Campbell, and R. Betti, Phys. Plasmas **23**, 022702 (2016).
[23]P. F. Knapp, M. R. Gomez, S. B. Hansen, M. E. Glinsky, C. A. Jennings, S. A. Slutz, E. C. Harding, K. D. Hahn, M. R. Weis, M. Evans, M. R. Martin, A. J. Harvey-Thompson, M. Geissel, I. C. Smith, D. E. Ruiz, K. J. Peterson, B. M. Jones, J. Schwarz, G. A. Rochau, D. B. Sinars, R. D. McBride, and P.-A. Gourdain, Phys. Plasmas **26**, 012704 (2019).
[24]T. J. Awe, K. P. Shelton, A. B. Sefkow, D. C. Lamppa, J. L. Baker, D. C. Rovang, and G. K. Robertson, Rev. Sci. Instrum. **88**, 093515 (2017).